

Quantum dynamics simulation of intramolecular singlet fission in covalently linked tetracene dimer

Sam Mardazad,¹ Yihe Xu,² Xuexiao Yang,² Martin Grundner,¹ Ulrich Schollwöck,¹
Haibo Ma,² and Sebastian Paeckel¹

¹*Arnold Sommerfeld Center of Theoretical Physics, Department of Physics,
University of Munich, Theresienstrasse 37, 80333 Munich,
Germany^{a)}*

²*School of Chemistry and Chemical Engineering, Nanjing University, Nanjing 210023,
China*

(*Electronic mail: sebastian.paeckel@physik.uni-muenchen.de)

(*Electronic mail: haibo@nju.edu.cn)

(*Electronic mail: sam.mardazad@physik.uni-muenchen.de)

(Dated: 2 August 2021)

In this work we study **singlet fission** in tetracene para-dimers, covalently linked by a phenyl group. In contrast to most previous works, we account for the full quantum dynamics of the combined excitonic and vibrational system. For our simulations we choose a numerically unbiased representation of the molecule's wave function enabling us to compare with experiments, exhibiting good agreement. Having access to the full wave function allows us to study in detail the post-quench dynamics of the excitons. Here, one of our main findings is the identification of a time scale $t_0 \approx 35$ fs dominated by coherent dynamics. It is within this time scale that the larger fraction of the **singlet fission** yield is generated. We also report on a reduced number of phononic modes that play a crucial role for the energy transfer between excitonic and vibrational system. Notably, the oscillation frequency of these modes coincides with the observed electronic coherence time t_0 . We extend our investigations by also studying the dependency of the dynamics on the excitonic energy levels that, for instance, can be experimentally tuned by means of the solvent polarity. Here, our findings indicate that the **singlet fission** yield can be doubled while the electronic coherence time t_0 is mainly unaffected.

^{a)}Munich Center for Quantum Science and Technology (MCQST), Schellingstrasse 4, 80799 München, Germany

I. INTRODUCTION

Singlet fission (SF) is a spin-allowed photophysical process that generates two triplet excitons from one singlet excited state¹⁻⁴. It can realise **multiple exciton generation (MEG)** and provide longer-ranged exciton transport inside a semiconductor (typically of the order of μm for triplets compared to $\sim 10\text{nm}$ for singlets^{5,6}). This process gives rise to an increase in the charge-carrier to radiation ratio, resulting in a net increase of efficiency for organic semi-conductor based photo-voltaics. **SF** has therefore shown the potential to surpass the upper bound of solar cell efficiency of 33%, set by the Shockley-Queisser limit and, hence, has attracted great attention^{7,8}.

Previous theoretical and experimental studies⁹⁻¹⁸ investigated the mechanism behind **SF** and distinguished between coherently driven and thermally activated **SF**, where only the latter exhibits a strong temperature dependence. The different mechanisms happen on different time-scales, namely up to 700fs for coherently driven **SF**¹⁸ and $> 1\text{ps}$ for thermally activated **SF**¹⁷. Unlike widely studied **intermolecular singlet fission (xSF)** systems of crystalline tetracene and pentacene, covalently linked chromophore dimers allow much easier control of inter-chromophore orientation and interaction for **intramolecular singlet fission (iSF)**^{10,19}. This is achieved by chemical modification of the bridging group and tuning of the solvent environment. For example, Wang et al., recently reported fast **iSF** within 10ps in covalent tetracene dimers linked by phenyl groups as in Figure 1 and illustrated its temperature dependence and significant solvent polarity effects⁹.

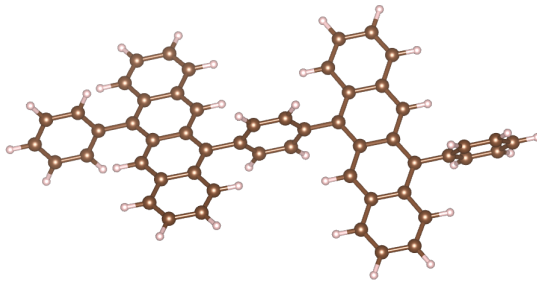


FIG. 1. Molecular structure of the tetracene para-dimer.

It is nowadays well-known that a pure electronic description is insufficient to describe these processes correctly^{2,3,20-22}, suggesting the necessity of the incorporation of molecular vibrations into theoretical considerations. The main obstacles for realistic calculations are, besides others, a faithful microscopic modelling of the coupling between electronic states and vibrational degrees of

freedom, as well a full quantum mechanical treatment of their coupled dynamics. Previously, due to the lack of knowledge of the full coupling Hamiltonian, the first problem has been addressed by investigating the effect of successive elimination of vibrational degrees of freedom in order to identify the relevant modes^{11,12}. To accomplish a faithful simulation of the quantum dynamics following the light excitation, a variety of methods has been applied, including [multi-configurational time-dependent Hartree \(MCTDH\)](#)^{23–25}, Redfield theory^{26,27} and [time-dependent wave packet diffusion \(TDWPD\)](#)²⁸. However, despite numerous investigations, there has been few numerically unbiased simulations of a full microscopic Hamiltonian that is generated from first principles for both, electronic molecular and vibronic degrees of freedom^{12,29}. Additionally, most time-evolution schemes used so far are either valid only in the weak-coupling regime (Redfield theory) or require an ad-hoc decomposition of the vibrational degrees of freedoms into clusters^{11,12} (multi-layer-[MCTDH](#)^{30,31}).

Recently, Chin, et al. applied [tree tensor-network states \(TTNSs\)](#)³² to model [xSF](#) in [13,13'-bis\(mesityl\)-6,6'-dipentacenyl \(DP-Mes\)](#) dimers. Exploring an involved numerical procedure, they effectively computed the non-perturbative real-time dynamics of exponentially large vibronic wave functions of real molecules. In this work, we attempt to adopt another novel one-dimensional tensor network method to simulate [iSF](#) dynamics in realistic chemical systems. Contrary to the procedure presented in [32](#), the above mentioned limitations are overcome by a conceptually much simpler yet powerful and numerically well-controlled procedure, as described in the following. First, we compute the spectral density from ab-initio multireference quantum chemical calculations and determine the effect of the molecule's vibrational modes on the electronic overlap integrals to obtain an effective model, capturing the coupling between electronic states and vibrations. Employing the resulting microscopic model, we perform a simulation of the full post photo-excitation quantum dynamics using a novel method from tensor networks³³. In particular, this method allows for the description of many bosonic degrees of freedom with a large number of internal states by dynamically selecting the relevant bosonic modes. The resulting, advanced numerical simulations enable us to achieve good agreement with experimental data measured for the tetracene para-dimer, covalently linked by a phenyl group. Furthermore, we are able to unambiguously identify the relevant vibrational modes dominating the post-excitation dynamics by studying the energy transfer within the molecule. Our findings of the coherent and incoherent dynamics' time scales are in very good agreement with previous investigations^{11,12}. However, here these results are based on a realistic microscopic modelling of the full molecule's dynamics. Having ac-

cess to the molecule’s full wave function, we study the connection between energy transfer into the vibrational system and phonon-assisted, coherently driven **iSF**. Our analysis reveals a competition between an initial coherent dynamics generated by the vibrational system, and its suppression due to the formation of heavy exciton-phonon quasi particles. Finally, being able to perform realistic simulations, we tuned experimentally relevant parameters such as the solvent polarity to identify the parameter regime generating the largest **SF** yield.

The scope of this paper is as follows. In section **II** we introduce a Hamiltonian for exciton-phonon mixtures describing our system adequately. This employs a global coupling of non-local vibrations to excitonic degrees of freedom. In section **III** we briefly sketch the new method and exhibit performance advantages. Furthermore, we are going to discuss the necessity for large local Hilbert spaces in simulating these types of model. Accounting for the rapid development of tensor network techniques for large Hilbert space sizes, we also briefly elaborate on why standard, widely used methods may not be appropriate here and discuss our approach in the context of the **TTNS** formulation introduced by Chin et al.³². Finally we present the simulated **iSF** dynamics in section **IV**. These involve comparison to experiment, as well as detecting the phononic modes dominating the energy transfer. We find a total triplet population between 14 % to 25 % depending on the solvent, compareable to the order of magnitude of experimental findings, i.e. 21 %⁹. Eventually, we investigate the tuning of experimental parameters, i.e. the solvent polarity, on the total triplet yield.

II. MODEL

To model the **SF** process, we describe the diabatic electronic states coupled to vibrational modes by means of a Frenkel-exciton-Hamiltonian^{34,35}

$$\hat{H} = \sum_{ij} V_{ij} \hat{c}_i^\dagger \hat{c}_j + \sum_I \omega_I \hat{b}_I^\dagger \hat{b}_I + \frac{1}{\sqrt{2}} \sum_{ij,I} g_{ij,I} (\hat{b}_I^\dagger + \hat{b}_I) \hat{c}_i^\dagger \hat{c}_j, \quad (1)$$

where lower-case indices i, j correspond to excitonic states and upper-case indices I denote vibrational modes. Here, $\hat{c}_i^{(\dagger)}$ correspond to the usual excitonic creation and annihilation operators while $\hat{b}_I^{(\dagger)}$ create and annihilate phonons. The diagonal elements ($i = j$) of V_{ij} resemble the energies of the excitonic states, while the off-diagonals ($i \neq j$) corresponds to the couplings among them. ω_I is the frequency of the vibration mode I and $g_{ij,I}$ represents the coupling between the excitonic Hamiltonian and vibrational modes I . We can distinguish between diagonal and off-di-

TABLE I. Excitonic Hamiltonian elements V_{ij} and their corresponding thermal fluctuations σ_{ij} (defined in Equation (3)) at 300 K in units of eV. The first entry per cell is V while the second denotes σ for the given pair of diabatic states i, j .

	LE ₁ ⟩		LE ₂ ⟩		CT ₁ ⟩		CT ₂ ⟩		TT⟩	
LE ₁ ⟩	2.9635	0.279	-0.0857	0.035	0.0431	0.039	-0.0535	0.052	0.0002	0.000
LE ₂ ⟩			2.9637	0.280	0.0535	0.052	-0.0431	0.040	-0.0002	0.000
CT ₁ ⟩					3.3645	0.276	-0.0007	0.001	-0.0612	0.055
CT ₂ ⟩							3.3645	0.276	-0.0612	0.055
TT⟩									3.1493	0.516

agonal coupling here as well. In order to describe our system adequately, we use five diabatic states. These are the two **locally excited (LE)** states LE₁ and LE₂, the two **charge transfer (CT)** states CT₁ and CT₂, and the **triplet pair (TT)** state. While the **LEs** model the electronic excitation in the dimer subsystems, the **CTs** are energetically high lying states that, if occupied, represent intermediate cationic or anionic molecular states³⁶. By initializing the system in one of the **LE** states (or a coherent superposition) we model a photo-excitation. It was previously shown that the localised triplets in the chromophore units can be interpreted as an electron-hole bound state⁴. However these triplets in each subsystem are correlated into an overall singlet state^{2,37} which we call **TT**. The dissociation of the **TT** state into locally separated triplets is a topic on its own and not part of this investigation^{36,38}. The details of the construction of these five diabatic states from **state averaged complete active space self consistent field (SA-CASSCF)** excited state calculations can be found in appendices **A** and **D**. The diabatic exciton matrix elements V_{ij} thus obtained are shown in Table I. Note that the multi-exciton **TT** state is optically dark^{4,39}. Furthermore the coupling between **LE** and **TT** is almost zero and, thus, direct conversion is strongly suppressed. This originates from the fact that the direct process corresponds to a double-electron transfer. The related two-electron integrals, between **HOMOs/LUMOs** of different groups or molecules, are usually vanishingly small^{3,16,40}. However, the couplings between **CT** and **TT** or **LE** are relatively large (40–60 meV). This suggests a possible indirect superexchange **iSF** path (**LE**→**CT**→**TT**)^{41–45}. It should be mentioned that due to the lack of dynamical correlation in the **CASSCF** calculations, the diagonal entries of the excitonic matrix V_{ij} may be inaccurate. Therefore we tune the **LE** and **TT** energies to fit the peak position of experimental absorption spectra. Furthermore the energies

of CT are obtained from a linear search within the range of 3.0645–3.5645 eV using Redfield dynamic simulations²⁷. Details about this procedure can be found in appendix D.

To estimate the coupling strength between excitonic states and vibrations we calculate the spectral density according to

$$J_{ij}(\omega) = \sum_I g_{ij,I}^2 \delta(\omega - \omega_I), \quad (2)$$

and the temperature-dependent fluctuations of the excitonic Hamiltonian elements using

$$\sigma_{ij}^2 = \int_0^\infty d\omega J_{ij}(\omega) \coth \frac{\omega}{2kT}. \quad (3)$$

The details of the methodology for evaluating the exciton-phonon couplings and the graphical illustrations of some essential vibrational modes can be found in appendices B and C. Results are shown in Table I and Figure 2. From the selected spectral density displayed in Figure 2, we can see that for diagonal elements, there are high-frequency modes near 1400 cm⁻¹ dominating the coupling. The remaining spectral densities for other couplings can be found in appendix C. Modes no. 184 (1409.61 cm⁻¹) and no. 185 (1411.18 cm⁻¹) account for these peaks. They change the backbone of the tetracene chromophore unit (see appendix B). This will influence the **molecular orbital (MO)** coefficients and integrals substantially and changes the energy of diabatic states consequently. At the same time the lower frequency mode at 415 cm⁻¹, which mainly twists the plane of the bridging phenyl group (see appendix B), mostly contributes to the coupling in off-diagonal elements. Under this oscillation the tetracene group remains unaltered and therefore the diagonal elements are less sensitive to this mode. The off-diagonal elements, however, depend on the overlap between orbitals from different tetracene chromophore units. The latter are dominated only to a small part by the orbitals in the bridge, because the tetracene groups are far away from each other. Consequently, twisting the bridge will change only the off-diagonal elements significantly. Furthermore, the lowest frequency mode around 7 cm⁻¹ also contributes to off-diagonal elements because it changes the dihedral angle between the planes of two tetracene units.

In order to maintain numerical feasibility we have to pick the relevant vibrational modes of the 88 atomic molecule. Out of the 258 vibrational modes we neglect 181 which trigger relative fluctuations smaller than 0.1%. We also discard the modes with frequencies below 10 cm⁻¹ since their oscillation periods are longer than 200 fs. This timescale is set by the time-range of our quantum dynamics simulation. Finally, we couple the remaining 76 modes, ranging from frequencies 10.18 cm⁻¹ (0.0013 eV) to 1714.2 cm⁻¹ (0.2125 eV), to the excitonic system.

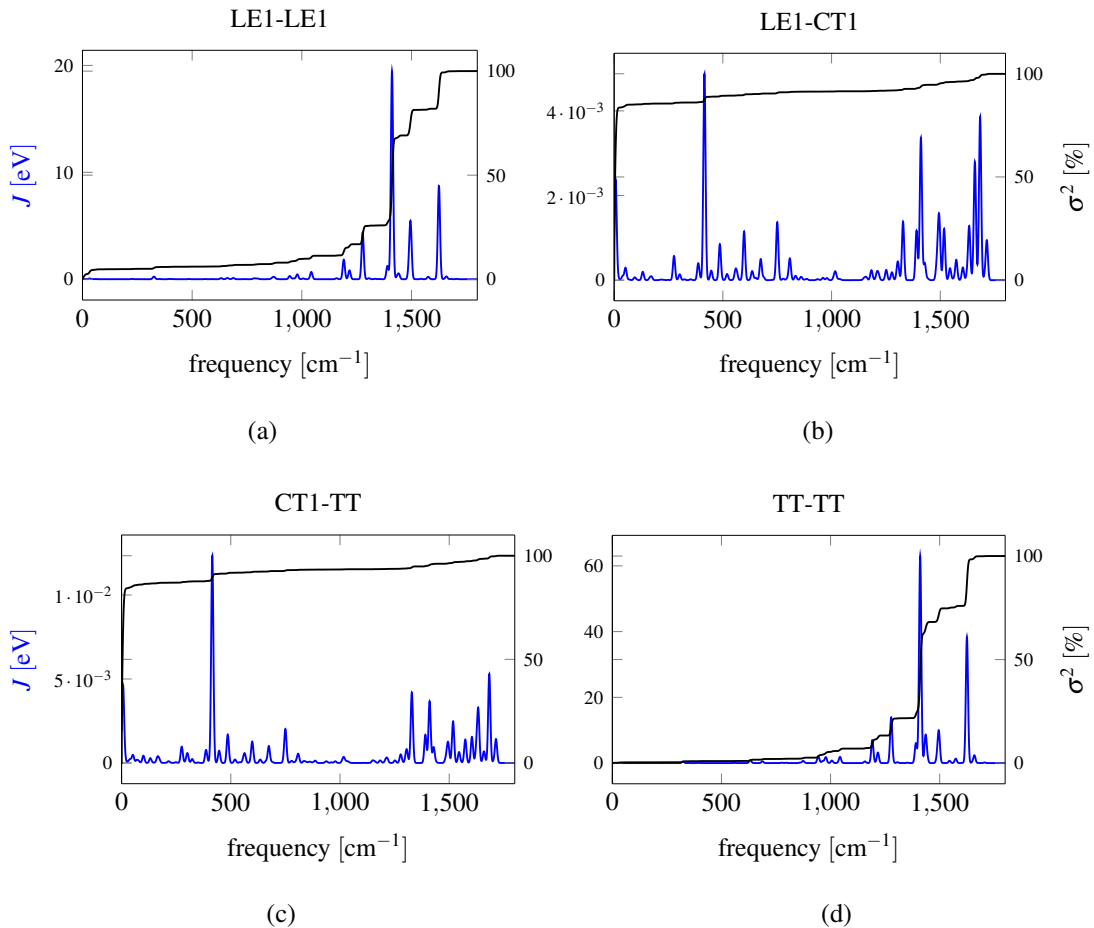


FIG. 2. Spectral density (blue, left axis) and accumulated fluctuations (black, right axis) of selected excitonic Hamiltonian terms at room temperature.

III. METHODS

Simulating the full quantum dynamics of Equation (1) requires a careful and well-converged treatment of the relevant vibrational modes. For that reason we exploit a [matrix-product state \(MPS\)](#) representation^{46–48} of the full quantum many-body wavefunctions to represent the time-evolution of the photo-excited system. The major challenge is the fact that each vibronic mode in principle requires an infinite number of internal degrees of freedom. For practical purposes we need to truncate the local Hilbert space dimensions to a large, but finite, number $d = n_{\text{ph}} + 1$. In doing so, care must be taken to choose the local dimensions large enough such that the dynamics is well-behaved. Otherwise, the system will notice the upper limit of the allowed vibrational mode occupations. This truncation needs to be balanced with computational cost scaling as $O(d^3)$ in the local dimension for the two-site [time dependent variational principle \(TDVP\)](#) method, which

we used in our calculations to perform the time evolution^{49,50}. The numerical calculations were carried out using the SyTen toolkit⁵¹.

We overcome these issues by employing the newly developed method of [projected-purification \(PP\)](#)^{33,52}. Within this approach we restore the $U(1)$ -particle number conservation symmetry by doubling the size of the (phononic) system. Furthermore, we introduce a dynamical procedure to truncate the local phononic Hilbert space dimensions d adaptively by the choice of our truncated weight ($\delta = 1.0 \times 10^{-8}$). This enables us to treat large local Hilbert spaces with $n_{\text{ph}} = 63$ very efficiently with the approximation being well-controlled by the maximally allowed sum of discarded Schmidt values.

A. Representing the vibrational modes

Let us briefly summarise the key points of this procedure. We start with a wave function expanded in a local basis labeled by irreducible representations of a global operator \hat{N}

$$|\psi\rangle = \sum_{n_1 \dots n_L} c_{n_1 \dots n_L} |n_1 \dots n_L\rangle. \quad (4)$$

Here L corresponds to the total number of single particle orbitals and the n_i run from $\{0, \dots, d-1\}$. Exploiting global $U(1)$ symmetries typically provides a significant speedup in numerical simulations⁵³, however, the number of phonons is not conserved in Equation (1). We circumvent this problem by introducing an auxiliary environment Hilbert space, which is a copy of the original one:

$$|\psi\rangle = \sum_{\substack{n_1 \dots n_L \\ \bar{n}_1 \dots \bar{n}_L}} c_{n_1 \dots n_L \bar{n}_1 \dots \bar{n}_L} |n_1 \dots n_L\rangle |\bar{n}_1 \dots \bar{n}_L\rangle. \quad (5)$$

Here pure indices n_j corresponds to physical degrees of freedom, while those carrying a bar \bar{n}_j involve the auxiliary space. We further introduce the gauge condition

$$c_{n_1 \dots n_L \bar{n}_1 \dots \bar{n}_L} = 0 \quad \Leftrightarrow \quad \forall n_i + \bar{n}_i \neq n_{\text{ph}} = d - 1. \quad (6)$$

This transforms Equation (5) into

$$|\psi\rangle = \sum_{n_1 \dots n_L} c_{n_1 \dots n_L, n_{\text{ph}}} |n_1 \dots n_L\rangle |n_{\text{ph}} - n_1, \dots, n_{\text{ph}} - n_L\rangle, \quad (7)$$

which happens to be an eigenstate of $\hat{N} + \hat{\bar{N}}$, i.e., the total particle number operator expanded to the enlarged Hilbert space, with particle number Ln_{ph} . Figure 3a illustrates this idea, showing

exemplary the effect of the gauge constraints at the example of the two lowest excitations of a vibrational mode. It can be shown³³ that there exists a bijective mapping between the basis in the original Hilbert space and the basis of the doubled one. Note that the subspace spanned by all basis states $\{|n_1 \dots n_L\rangle |n_{\text{ph}} - n_1, \dots, n_{\text{ph}} - n_L\rangle\}_{n_1, \dots, n_L}$ has the same dimension as the original one. We also map arbitrary global operators to the purified Hilbert space, by substituting creation and annihilation operators with

$$\hat{b}_i = \sum_{n=0}^{n_{\text{ph}}-2} \sqrt{n+1} |n\rangle_{ii} \langle n+1| \otimes |n+1\rangle_{ii} \langle n| \quad (8)$$

$$\hat{b}_i^\dagger = \sum_{n=0}^{n_{\text{ph}}-2} \sqrt{n+1} |n+1\rangle_{ii} \langle n| \otimes |n\rangle_{ii} \langle n+1| \quad (9)$$

in terms of the operators breaking the global $U(1)$ symmetry. The remaining operators are tensored with identities in the auxiliary space. With this representation of \hat{H} one always stays within the purified sub-manifold³³.

Adopting this representation, we have obtained a formal global $U(1)$ symmetry for the phonon system that is not particle number conserving, at the cost of introducing a reservoir degree of freedom for each bosonic orbital, as shown in Figure 3b. Instead of treating a few huge matrix blocks, we can now compute with a lot of small ones. We exploit the potentially large number of blocks by parallelizing contractions over the symmetry blocks. Furthermore, we make careful use of the real space parallel TDVP algorithm⁵⁴ for some of the solvent dependent calculations.

Importantly, the PP mapping allows to variationally optimise in the space of retained optimal phononic modes by the tuning of one parameter, the truncated weight during the singular value decomposition (SVD). This can be understood by means of the relation between the retained singular values s_τ during the decimation process of density matrix renormalization group (DMRG)⁴⁶ and the diagonal elements of the reduced density matrix (RDM) of a single bosonic site ρ ³³,

$$\sum_{\tau} (s_\tau^n)^2 = \rho_{nn}. \quad (10)$$

Here the index n indicates the singular values belonging to the corresponding irreducible representation. Discarding the smallest singular values fulfilling $\sum_{n,\tau} (s_\tau^n)^2 \leq \delta$ corresponds to eliminating occupation number elements ρ_{nn} not required for an adequate description of the state. Hence, the initial local Hilbert space dimensions d of the vibronic modes are truncated to significantly smaller values, rendering the simulations numerically feasible. During the dynamics, the truncation process of the state enforces the system to keep only the modes required for an adequate

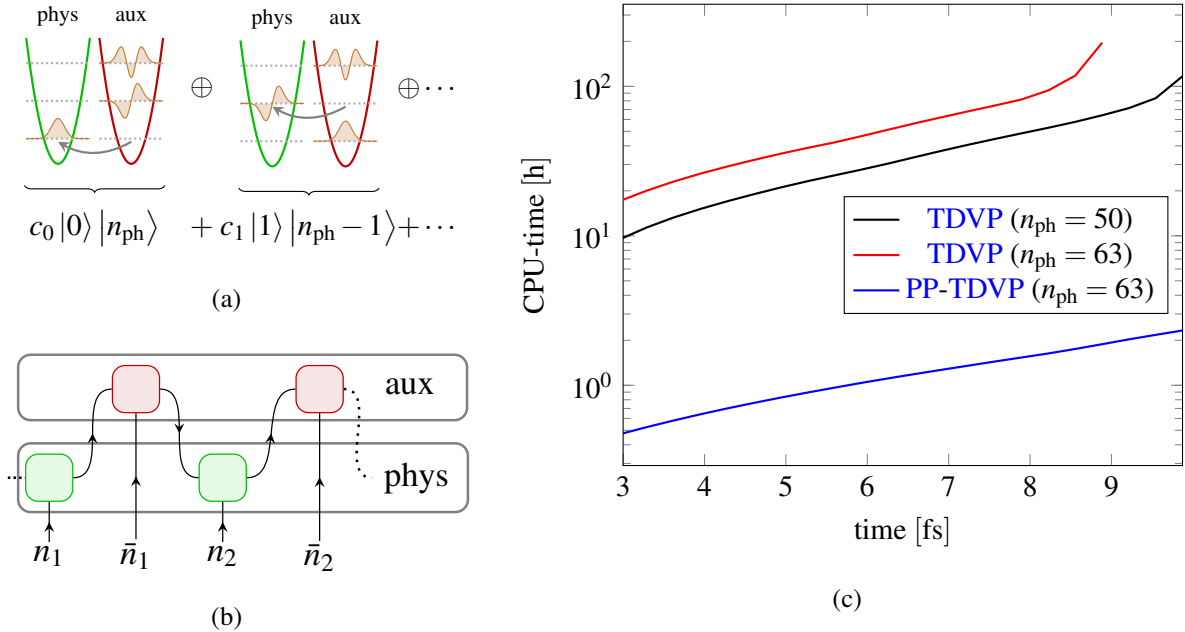


FIG. 3. (a) illustrates the effect of the PP mapping. Each vibronic degree of freedom is accompanied with an auxiliary site. Vibronic excitations are modeled by moving occupations from the auxiliary to the physical system, introducing a global $U(1)$ symmetry. This symmetry can be exploited by choosing a MPS representation that pairs up physical and auxiliary sites as shown in (b). The obtained CPU times for $n_{\text{ph}} = 50, 63$ without the PP-mapping and for $n_{\text{ph}} = 63$ with PP are displayed in (c). All calculations were carried out on an Intel[®]Xeon[®]Gold 6130 CPU (2.10GHz) with 32 threads. Note the logscale on the y-axis.

approximation of the state (i.e. with sufficient weight).

The restored global $U(1)$ symmetry of the phononic system combined with this truncation scheme results in a highly diminished memory requirement and, more importantly, reduction of CPU time by a factor 100-1000, due to decomposition and parallelisation respectively, as is shown in Figure 3c. We compare the total CPU times during the initial stage of the dynamics, following a photo excitation of a bright exciton with and without exploiting the PP mapping and for different local Hilbert space dimensions d in case of the trivial phonon representations. Note that in the conventional approach the memory requirements grow rapidly, causing a breakdown of the simulations without the PP mapping after times of only 8.5 fs or 9.9 fs, respectively .

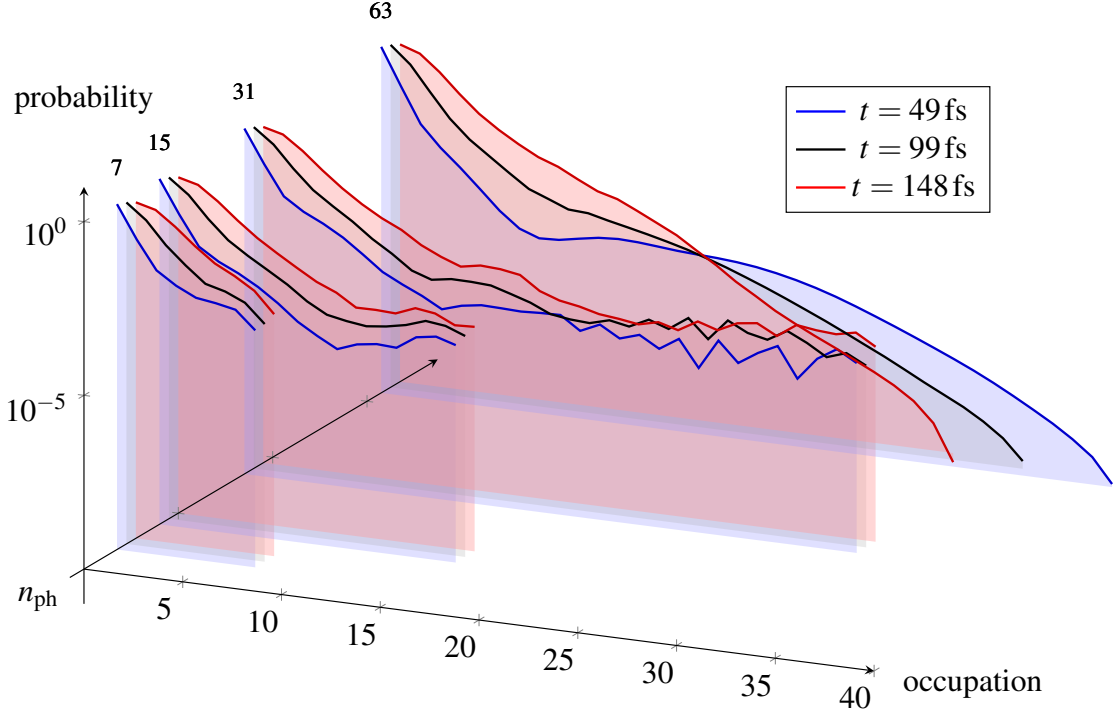


FIG. 4. Excitation probability for occupations of phonon mode no. 184 for different times during the dynamics.

B. Numerical stability and effects of insufficiently large vibrational Hilbert spaces

Treating the exciton-phonon coupling in a numerically controlled manner is crucial in order to describe the dynamics of the vibrational modes correctly. For that purpose, we monitor the probability of different phonon occupation numbers by calculating the **RDM** during the time evolution. The **RDM** with respect to a vibronic mode J is obtained by tracing out all degrees of freedom from the total density operator except for the target mode J

$$\hat{\rho}_J = \text{tr}_{\{I\} \setminus J} |\Psi\rangle \langle \Psi|, \quad (11)$$

where $\{I\}$ is the set of all phononic modes. Exemplary, we investigate the dynamics of a particular phonon mode (no. 184) which plays a dominant role in the excitonic dynamics (see also Figure 2 and appendix C). In order to clarify the role of the truncated local Hilbert space we systematically tune the maximally allowed phonon numbers, i.e. $n_{\text{ph}} = 7, 15, 31, 63$. The result for the vibrational mode no. 184 is shown, in exemplary fashion, in Figure 4. It shall be mentioned that intermediate sizes, like e.g. $n_{\text{ph}} = 23$, show the same behaviour as the others and are therefore left out for clarity. We evaluate the **RDM** at three distinct times after the photo excitation, namely 49 fs, 99 fs

and 148 fs. We observe that the dynamics of the probabilities to excite only a small number of ~ 10 vibrational quanta is correctly described for all maximally allowed phonon numbers n_{ph} . However, inspecting the tail of the excitation probabilities, significant deviations are visible at the order of $\delta\rho_{J,nn>10} \sim 10^{-5}$, as long as $n_{\text{ph}} < 63$. This translates into a failure of describing the relaxation of the initially excited phonon modes in the scope of the time evolution, if the local Hilbert space dimensions are too small. We relate this problem to the contribution of the higher excited vibrational modes to the overall time evolution operator $e^{-i\hat{H}t}$. Here, the vibrational energy contributions of \hat{H} scale as $\langle \hat{n}_J \rangle \propto \sum_n n \times \rho_{J,nn}$. Inspecting Figure 4 we find that for $n_{\text{ph}} < 63$ the error is dominated by excitation probabilities of $\rho_{J,nn=10-30}$, i.e., an overall error of $\sum_{n=10}^{30} n\delta\rho_{J,nn} \sim 10^{-3}$. This means the reported deviations contribute overall errors in the time evolution scaling as $\sim 10^{-3}$ in the case of mode no. 184.

These observations clearly show that the higher occupation numbers of the vibrational modes can make up for non-negligible contributions to the **iSF** quantum dynamics, even though the mean occupation and displacement of all vibrations can be quite small. This implies the necessity of employing a large, maximally allowed phonon number n_{ph} per lattice site. However, since throughout the simulations the system dynamically chooses the actually required phonon Hilbert space dimension we are able to truncate away unnecessary modes without any additional numerical effort.

C. Relation to other tensor network techniques

Finally, we comment briefly on why two other common tensor network methods appear unsuitable for a full quantum dynamics simulation of the current problem (for a more detailed comparison see⁵²). We do not discuss **MCTDH** here, since it was extensively explained in previous works^{11,23,24,29-31}.

The **pseudo-site (PS) DMRG** unfolds the local Hilbert spaces of the phononic part of the system into auxiliary sites and encodes the phonon occupations into a binary representation^{55,56}. Thereby, the computational complexity originating from the large local Hilbert space dimensions is reduced drastically at the cost of introducing long-ranged couplings. The **PS DMRG** has been applied successfully to study out-of-equilibrium-dynamics of Holstein models⁵⁶. However, in these systems the electron-phonon couplings are strictly local. For the tetracene the situation is quite different as the diabatic states couple highly non-locally to the vibrational degrees of freedom. The arising long-range couplings span the whole system such that combined with the binary encoding of the

phononic Hilbert spaces the calculations with $n_{\text{ph}} = 63$ would require a total system size of 461 orbitals, which are coupled over the whole range of lattice sites. It has been demonstrated⁵² that already for groundstate calculations, the convergence of **DMRG** algorithms can be quite challenging for such a large number of lattice sites in the **PS** representation. In an out-of-equilibrium setup we expect these problems to become even more severe.

The **local basis optimization (LBO)** is another very successful method based on rotating the local phononic Hilbert space representations into an optimized basis, allowing for a truncation of the required large local dimensions^{57,58}. This effective compression generates a significant speedup in the tensor contractions and has been applied to study the dynamics of coupled electron-phonon system following a global quench^{58,59}. However, in contrast to groundstate calculations, the optimization of the local basis has to be performed at each time step during the time evolution to maintain the optimal description of the vibrational degrees of freedom⁶⁰. As a consequence, only parts of the effective Hamiltonian can be represented in the optimised basis, the remainder still requires the full local Hilbert space dimension $d = n_{\text{ph}} + 1$ of the original phononic Hilbert space. To be more precise, the most expensive numerical operation is the application of the effective Hamiltonian which scales as d^3 in the local dimension. Within the **LBO** scheme, this translates into a scaling $d^2 d_{\text{eff}}$ where d_{eff} is the dimension of the optimised local basis representation. Thus, the numerical costs are reduced at the most by a factor of d_{eff}/d . Comparing this estimation for the speedup of the **LBO** method with the speedup presented in Figure 3c we find a significantly larger numerical efficiency exploiting the **PP** mapping.

Very recently³², a **TTNS** representation has been suggested to capture the non-local interactions between molecular electronic states and vibrational modes. As we have shown in section III B, it is inevitable to take into account a large number of excitations per vibrational mode. Exploring a **TTNS** representation, the idea is to reduce the numerical costs by grouping strongly correlated regions of the wavefunction, reducing the required bond dimension m . Assuming a two-site **TDVP** update (of a rank-3 tensor), the numerically most costly operations scale as $\mathcal{O}(m^3 d^2 w^2)$ or $\mathcal{O}(m^2 d^3 w^3)$, depending on the magnitude of the local dimension d and the bond dimension of the Hamiltonian representation w . Using the standard tensor-network representations, we found values of $w \sim \mathcal{O}(100)$ when constructing the Hamiltonian⁶¹, i.e., a bond dimension $m \sim \mathcal{O}(100)$ is an upper limit to maintain numerical feasibility of the time evolution, which was also used in 32. However, in a tensor-network representation the value of m is directly linked to the amount of correlations that can be captured by the corresponding bond. To resolve this conflict, entanglement

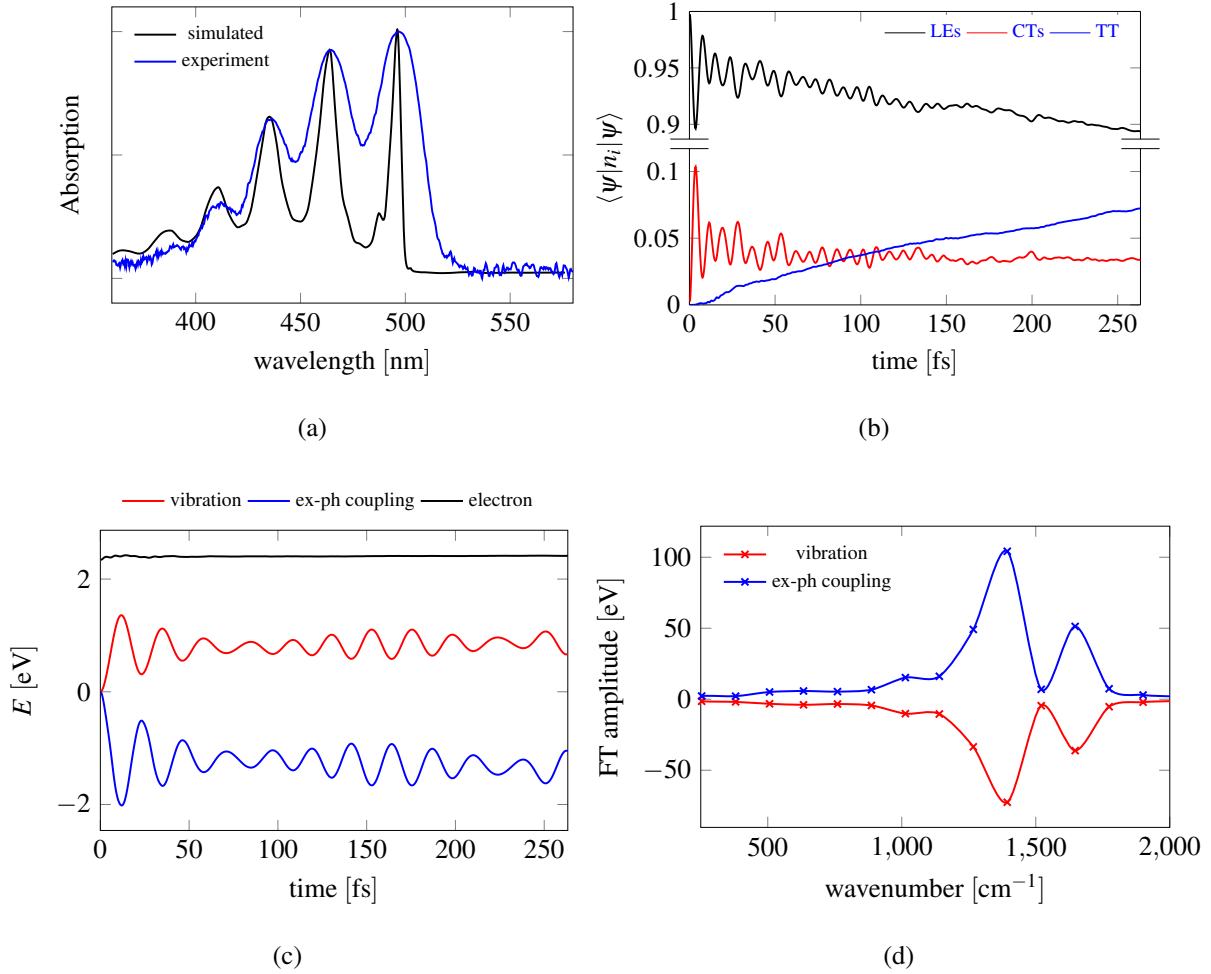


FIG. 5. (5a) Simulated absorption spectra compared with experiments. (5b) Population dynamics of different electronic states. The maximum TT population is 7.2%. (5c) The expectation value of different Hamiltonian components. (5d) The Fourier transform of (5c).

renormalization by means of machine learning based optimization strategies has been applied, to deduce a grouping of vibrational modes allowing the required reduction of m . In contrast, exploiting the artificial $U(1)$ symmetry introduced by the PP mapping, we find $w \sim O(10)$, enabling us to use $m = 6144$ without severe runtime losses while still working with a MPS representation, which is easy to adopt to various setups. Based on the previous discussion, we believe that combining the PP mapping with advanced entanglement renormalization could provide a further big leap.

IV. RESULTS

A. Absorption spectra and energy transfer

In order to verify the applicability of our model and methods we evaluate the absorption spectrum⁶²

$$I(\omega) \propto \text{Re} \int_0^{\infty} dt C(t) \exp[i\omega t - t/\tau] . \quad (12)$$

Here, $C(t)$ is the auto-correlation function

$$C(t) = \langle \chi(0) | \langle \varphi(0) | e^{-itH} | \varphi(0) \rangle | \chi(0) \rangle , \quad (13)$$

and τ is an appropriately short effective relaxation time. $|\varphi(0)\rangle$ is the initial excitonic state and $|\chi(0)\rangle$ the vacuum phononic state. Our system was prepared in the bright initial state configuration $|\varphi(0)\rangle = (|LE_1\rangle + |LE_2\rangle)/\sqrt{2}$. Analogous analysis for the localised and dark initial state can be found in appendix F.

The resulting calculation is displayed in Figure 5a. In order to resemble the relative magnitude of the 0-0 and the 0-1 peaks of the experimental spectrum⁹, the relaxation time is chosen to be $\tau = 230$ fs. We find the theoretical data capturing the main experimental features for the vibrationally resolved absorption spectrum. In particular, the position and relative magnitudes of the several dominating vibronic peaks are in excellent agreement. Furthermore, small wavelength features like e.g. a shoulder and a small peak (around ~ 380 nm and ~ 420 nm, respectively) are found correctly. However their absorption probability is slightly overestimated. We attribute the experimentally observed increased signal widths to the neglected phononic modes, which generate additional scattering processes between diabatic states and vibronic excitations.

In Figure 5b we see the dynamics of the populations of the diabatic states. Note that TT has a small delay time versus CT. This indicates that the indirect mechanism dominates the process. Both the populations of LE and CT show oscillations whose frequency is about 0.12 fs^{-1} . We find this value corresponding to the energy gap between two eigenstates of the pure excitonic Hamiltonian. It is these two eigenstates which account for over 96% of LE and CT when expanding the eigenbasis in terms of the components of the excitonic basis, i.e. they carry the main weight. This demonstrates how far the driving force from excitonic coupling is important for iSF in this system on short transient time-scales, in agreement with our findings from section IV B. Note

that the coherent oscillations disappear in the scope of the dynamics. This implies that the vibrational system is chosen large enough to achieve relaxation into an incoherent excitonic dynamics, contrasting previous works^{11,12}.

Having access to the full wave function, we are able to study the energy transfer between the excitonic and phononic system. For that purpose we evaluate the partial energies of the exciton and phonon system, as well as the coupling energy by separating Equation (1). The obtained time dependencies are displayed in Figure 5c. Most importantly, we find only few dominating oscillations in the coupling and vibrational energies at finite values, after an initial transient regime. As shown in Figure 5d, a Fourier transformation reveals that there are two frequencies dominating the energy conversion between exciton-phonon coupling and the phononic subsystem. They are located at around 1420cm^{-1} and 1620cm^{-1} , respectively. We identify these signals with vibrational modes as follows

1420cm^{-1} :	modes no. 184, 185 and 186 ,
1620cm^{-1} :	modes no. 209, 210 and 211 .

Note that all of these frequencies correspond to strong peaks in the spectral densities Figures 2a and 2d. The observation that the modes 184-186 are most relevant for the energy transfer can be related to the nature of these vibrational modes, i.e., they correspond to collective vibrations of the whole molecule's backbone (see appendix B). We note that previously¹¹ a study of the vibrational contributions to the excitonic dynamics found a similar relation for vibrational modes in the regime of 1420cm^{-1} . However, there the importance of these vibrational modes was determined by successively eliminating oscillation frequency windows.

B. Solvent and triplet energy dependence

In a subsequent stage we investigated the dependency of the triplet production on the energies of CTs and TT. Importantly, the CTs on-site energies can be tuned in the experiment by the solvent polarity⁶³. As shown in Figure 6 we scanned a whole parameter region shifting the energies. We measure the offsets of the CTs and TT from the values given in Table I by the gaps $\Delta E(\text{CT} - \text{LE})$ and $\Delta E(\text{CT} - \text{TT})$, respectively.

Most prominently, we find that lowering the energy of the CT states, i.e., increasing the solvent polarity, yields a larger TT population rate at the early stage. Moreover, the gained triplet pop-

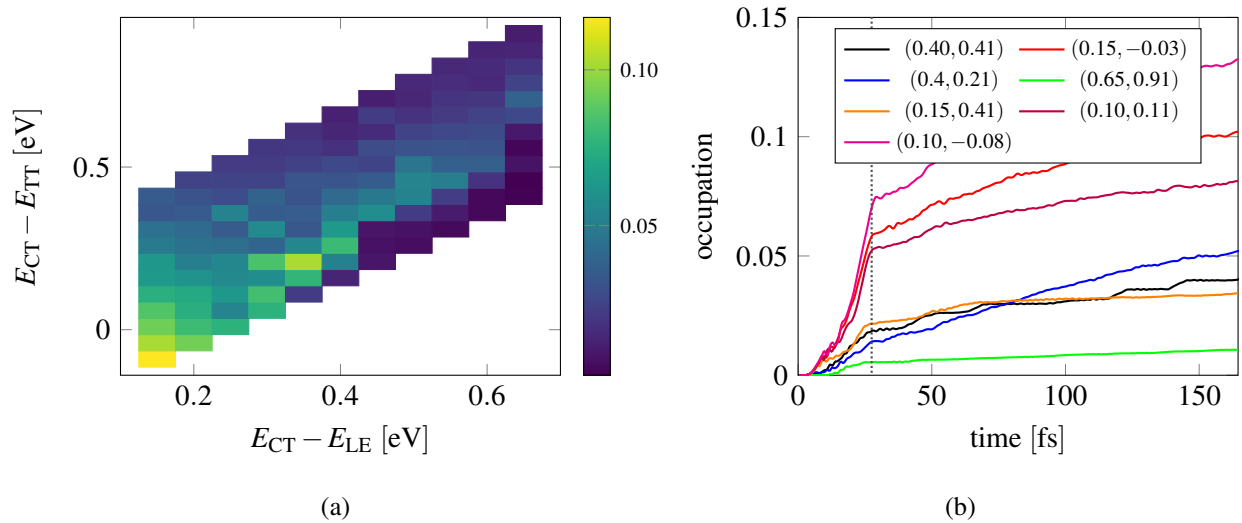


FIG. 6. Figure 6a shows the maximum TT population for different energies of the exciton states. Notice, that for each energy pair the maximum value is chosen, i.e. the occupations do not belong to the same point in time. Figure 6b gives the TT population with respect to the excitonic energies ($\Delta E(\text{CT} - \text{LE}), \Delta E(\text{CT} - \text{TT})$) in eV.

ulation can be elevated by increasing the energy of the TT state. Combining these observations we conclude that one dominating process for the TT yield is the relaxation of CT populations into the energetically closest diabatic states, suggesting the indirect iSF mechanism ($\text{LE} \rightarrow \text{CT} \rightarrow \text{TT}$). This picture is consistent with the observation that the TT production rate is strongly suppressed in the lower right corner of Figure 6a. Also, we note that the triplet yield obtained from the system parameters Table I matches experimental findings⁹, i.e., we find a relatively small value of 14%.

Previous studies^{11,12,64,65} found a finite time scale for the coherent dynamics. In order to determine this electronic coherence time, in Figure 6b we show the time-evolution of the TT population for selected limiting cases. We find a consistent change in the dynamics at $t_0 \sim 35$ fs where the slope of the TT production rate changes independent of the specific choice of the on-site potentials. As discussed in appendix G this can be addressed to a change of the nature of the excitonic dynamics. At times $t < t_0$ all excitonic states realise a coherently driven dynamics. However, at times $t > t_0$ this mechanism changes into a classically driven relaxation of mixed states of the LEs, CTs and TT subsystems. Previously, the coherent increase of TT population has been interpreted in terms of phonon-assisted hoppings employing Fermi's golden rule¹¹. However, we also found that the electronic coherence time roughly coincides with the oscillation time of the

dominating vibrational modes no. 184 and 185. In fact, their wavenumber of 1420cm^{-1} roughly translates to a period of 25 fs. Noting also that $\sim 2/3$, i.e., the dominating part of the **TT** population is generated during the coherent dynamics, this could create a competition between phonon assisted hoppings and the time scale in which these processes are possible. In appendix G we investigated the renormalisation of the excitonic couplings after rewriting the Hamiltonian using a Lang-Firsov transformation⁶⁶. Importantly, we find that the renormalisation of the couplings between the **TT** state and the remaining excitonic system changes from an enhancement to a suppression after $t_0 = (34.725 \pm 0.165)$ fs. It is a remarkable observation that the description of the phonon-assisted hopping in terms of polaron dynamics yields a perfectly matching prediction of the electronic coherence time. In this quasi particle picture, the coherent phonon-assisted hopping processes are blocked by the momentum transfer into the vibrational system. In fact, this momentum transfer creates a cloud of vibrations accompanying the excitonic states⁵⁸ and thereby increase the effective exciton mass. Our analysis further shows that within the coherent dynamics, the dominating hopping is between **CT** and **TT** states, pointing out the importance of the indirect hopping mechanism.

V. CONCLUSION AND OUTLOOK

We studied the **TT** production rate via **iSF** for a covalently linked tetracene dimer using a large-scale full quantum-mechanical treatment of the relaxation dynamics after photo-excitation. Our study extends the theoretical analysis conducted so far¹¹ by treating couplings between the diabatic states and the vibrational modes obtained from first principles. Incorporating a large number of molecular, vibrational modes we achieve a realistic description of the full molecule’s dynamics, following the photo-excitation. We obtain excellent agreement with experimentally observed absorption spectra and identify only a small number of vibrational modes, dominating the energy conversion between the different subsystems. Analysing the renormalisation of the exciton couplings in terms of exciton-phonon quasi particles, we can trace back the origin of the phonon-assisted coherent **TT** generation to an enhanced delocalisation of the created quasi-particle, which after some time transform into heavy, localised ones. A systematic variation of molecular parameters that can be related to the solvent polarity allows us to identify those regions in parameter space exhibiting the largest triplet yield.

As it is of special interest to raise the **TT** population to produce a high charge carrier yield, our

findings can be employed to identify promising manipulations of the molecular structure. Here, we suggest two pathways. First of all, decreasing the energy gaps between **CT** and **LE** or **TT** is crucial for producing higher **TT** yield. Our results indicate that both modifications of **CT** and **TT** energies mainly affect the overall scale of the triplet yield. Here, during the initial, coherent dynamics, a quick increase of the **TT** is observed which transforms to a classically driven relaxation, happening on time scales $t \gtrsim t_0 = 35$ fs. We note that the observed time scale for coherent dynamics is in agreement with previous studies, both theoretical and experimental^{9–18}. However, this time scale is very close to the oscillation period ~ 25 fs of the vibrational modes no. 184, 185 and 186 dominating the energy transfer between the excitonic and vibrational system. Therefore, our findings suggest a second route that, though experimentally more challenging, would be an increase of the electronic coherence time t_0 . Noting that the dominating fraction of the **TT** yield is generated from the initial, coherent dynamics, a combination of larger coherent times, i.e., a reduction of the frequency of the oscillations of the overall molecule’s backbone, with an increased solvent polarity could generate significantly larger **TT** occupations.

There are still many aspects to be further considered for future simulations of **SF** dynamics. First of all we might take into account more chromophore units. It was suggested recently that the spatial separation of the correlated triplets might be a crucial point in the harvest of a large yield⁹. Since the presented numerical framework can adaptively reduce the number of vibrational modes, it might be a promising tool to explore the dynamics of larger molecules, too. Additionally, finite temperature effects, which may become relevant for larger molecules⁹, can be incorporated by a thermofield approach, which is a standard technique for tensor network methods. From a methodical point of view, a direct comparison between established time-evolution schemes such as multi-layer **MCTDH**^{30,31} and the presented tensor network representation would be desirable. In particular, a faithful investigations of these different approaches could yield insights which method should be used to optimally describe **SF** dynamics. Furthermore, we believe that a combination of our representation of the vibrational degrees of freedom with **TTNS** and entanglement renormalisation techniques³² could open the path to study the full quantum dynamics of generic, large organic semi-conductors.

ACKNOWLEDGMENTS

We thank Dr. Xiaoyu Xie, Dr. Thomas Köhler and Prof. Uwe Manthe for helpful discussions. We acknowledge financial support by the Deutsche Forschungsgemeinschaft (DFG, German Research Foundation) under Germany’s Excellence Strategy-426 EXC-2111-390814868 (U.S.) and National Natural Science Foundation of China (Grant Number 22073045) (Y.X., X.Y., H.M.). Furthermore we acknowledge support from the Munich Center for Quantum Science and Technology (S.M., M.G., U.S and S.P.). All calculations made use of the SyTen toolkit⁵¹, some comparison benchmarks were performed using the SymMPS toolkit⁶⁷.

DATA AVAILABILITY STATEMENT

The data that support the findings of this study are available from the corresponding author upon reasonable request.

AUTHOR CONTRIBUTIONS

S.M. developed the idea, wrote the code and performed the calculations. Y.X. X.Y. and H.M. guided with chemical intuition to the chosen molecule. Y.X. and X.Y. did electronic structure calculations and the computation of the vibrational modes. S.M., Y.X. and S.P. interpreted the results and wrote the paper together. S.P. supervised the project and is one of the original authors of the main method. H.M., M.G. and U.S. discussed the results and helped interpret the data.

ADDITIONAL INFORMATION

Competing interests

The authors declare no competing interests.

Appendix A: Electronic Structure Calculation

We employ [CASSCF](#) with a $6 - 31G(d)$ basis set in order to calculate all the excited states involved in our [iSF](#) model due to the multi-excitation nature of [TT](#). The four orbitals near [highest](#)

occupied molecular orbital (HOMO) and lowest unoccupied molecular orbital (LUMO) are delocalised. Therefore we use the Pipek-Mezey method⁶⁸ on these orbitals to generate four localised ones (from HOMO-1 to LUMO+1). Each of them is confined in single tetracene chromophore. We construct all the diabatic states from the four localised orbitals and calculate all the excitonic Hamiltonian elements V_{ij} using complete active space configuration interaction (CASCI). All calculations are performed using the OpenMolcas package⁶⁹.

Here we only take into account the linear exciton-phonon coupling terms. We distort the whole molecule (at equilibrium geometry) along selected vibrational modes' displacement for $\pm 0.01 \text{ \AA}$. Then we calculate the excitonic Hamiltonian with the same procedure as mentioned above. With the Hamiltonian at three distinct points in space ($\pm 0.01 \text{ \AA}, 0 \text{ \AA}$), we can perform linear fitting of each elements V_{ij} and calculate the gradient. Note that the coupling $g_{ij,I}$ in Equation (A1) is connected to dimensionless displacement Q_I . One has to multiply the gradient by a factor of $\sqrt{\hbar/(m_I \omega_I)}$.

$$g_{ij,I} = \nabla_{Q_I} V_{ij}(\mathbf{Q}) \quad (\text{A1})$$

Appendix B: Vibrational modes

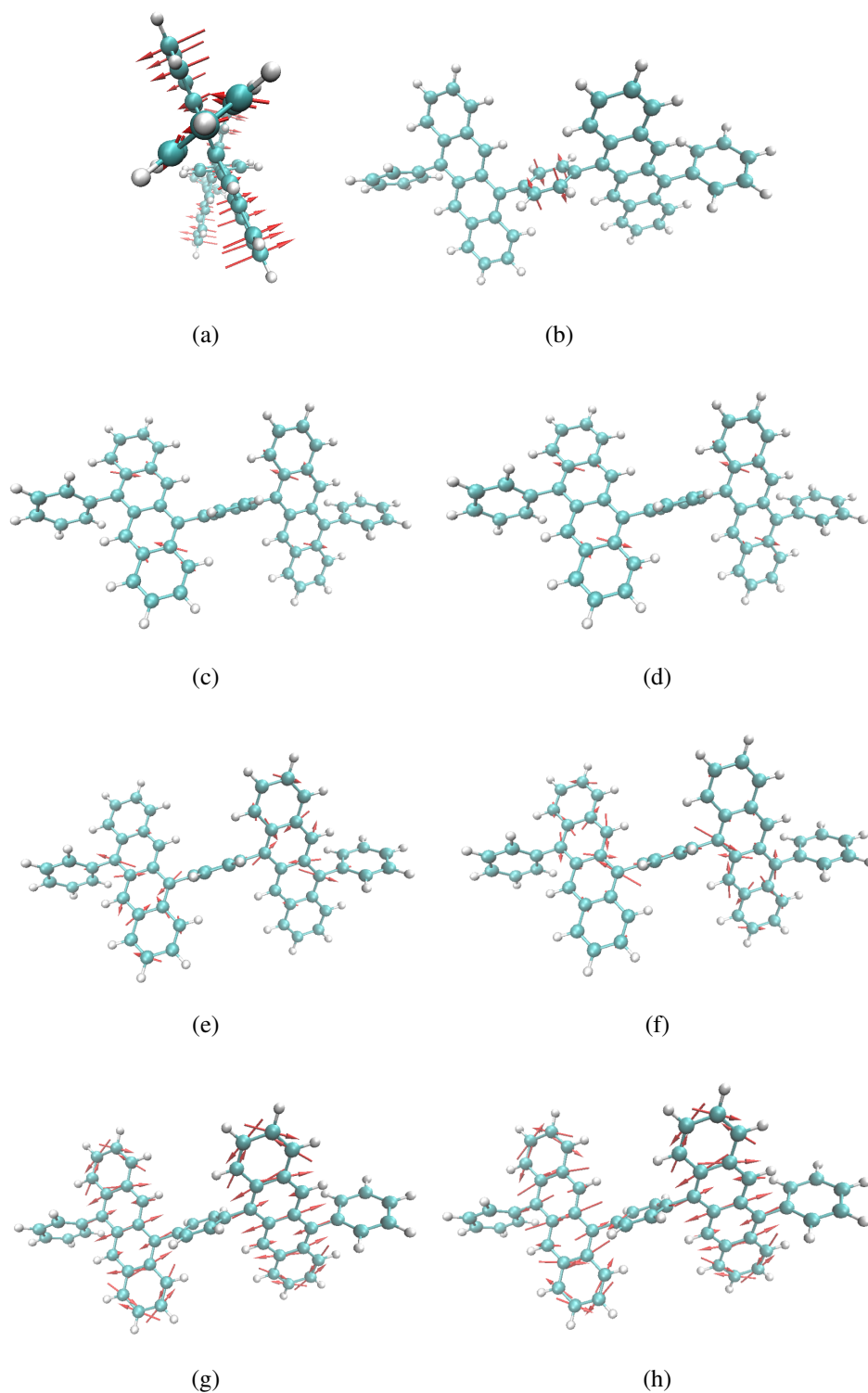


FIG. 7. Illustration of displacement vector of some essential vibrational modes: (7a) mode no. 1 (6.7 cm^{-1}). (7b) mode no. 45 (415.0 cm^{-1}). (7c) mode no. 167 (1277.0 cm^{-1}). (7d) mode no. 168 (1277.7 cm^{-1}). (7e) mode no. 184 (1409.6 cm^{-1}). (7f) mode no. 185 (1411.2 cm^{-1}). (7g) mode no. 210 (1624.9 cm^{-1}). (7h) mode no. 211 (1625.4 cm^{-1}).

Appendix C: Spectral Density Data

Spectral densities and fluctuations for some excitonic Hamiltonian elements which were not included in main text are displayed in Figure 8.

Appendix D: Redfield search

To obtain a reasonable shifted CT energy, we use Redfield theory^{26,27} to simulate the SF dynamics at the temperature of 300 K. In Redfield theory, the dynamics are described using

$$\frac{\partial \rho_{\alpha\beta}}{\partial t} = i(\varepsilon_\alpha - \varepsilon_\beta)\rho_{\alpha\beta} + \sum_{\alpha\beta\gamma\kappa} R_{\alpha\beta\gamma\kappa}\rho_{\gamma\kappa}, \quad (\text{D1})$$

where ρ is the density matrix of the excitonic states, and $\alpha, \beta, \gamma, \kappa$ label eigenstates of the excitonic Hamiltonian. Furthermore the Redfield tensor $R_{\alpha\beta\gamma\kappa}$ is defined as

$$R_{\alpha\beta\gamma\kappa} = \Gamma_{\kappa\beta\gamma\alpha}^+ + \Gamma_{\kappa\beta\gamma\alpha}^- - \delta_{\kappa\beta} \sum_{\lambda} \Gamma_{\alpha\lambda\lambda\gamma}^+ - \delta_{\gamma\alpha} \sum_{\lambda} \Gamma_{\kappa\lambda\lambda\beta}^-, \quad (\text{D2})$$

$$\Gamma_{\kappa\beta\gamma\alpha}^+ = \int_0^t d\tau \exp\{i(\varepsilon_\gamma - \varepsilon_\kappa)\tau\} \sum_j C_j(\tau) \langle \alpha|j\rangle \langle j|\beta\rangle \langle \gamma|j\rangle \langle j|\kappa\rangle, \quad (\text{D3})$$

$$\Gamma_{\kappa\beta\gamma\alpha}^- = \int_0^t d\tau \exp\{i(\varepsilon_\alpha - \varepsilon_\beta)\tau\} \sum_j C_j(\tau) \langle \alpha|j\rangle \langle j|\beta\rangle \langle \gamma|j\rangle \langle j|\kappa\rangle. \quad (\text{D4})$$

ε is the energy of the corresponding eigenstate and $C_j = \langle \delta\varepsilon_j(t) | \delta\varepsilon_j(0) \rangle$ is the energy fluctuation correlation function of the state j . We then tune the energy of CT within the range of 3.0645 – 3.5645 eV, according to the CASSCF results and the previous solvent effect investigations⁹, while fixing the energy of the other excitonic states. In order to perform the Redfield dynamics we choose the bright excited state as was discussed in the main text. Since $E_{\text{CT}} = 3.3645$ eV has the highest TT population we choose this as the TDVP input.

Appendix E: Numerical control parameters

In order to convince ourselves of the validity of the simulations we plot the maximum bond dimension and norm deviation in Figure 9. As we can see the localised and bright initial state have a rather moderate growth in the bond dimension. Therefore they are exact, with respect to the truncated weight of $\delta = 1.0 \times 10^{-8}$, until almost the end of the simulation time. In contrast the

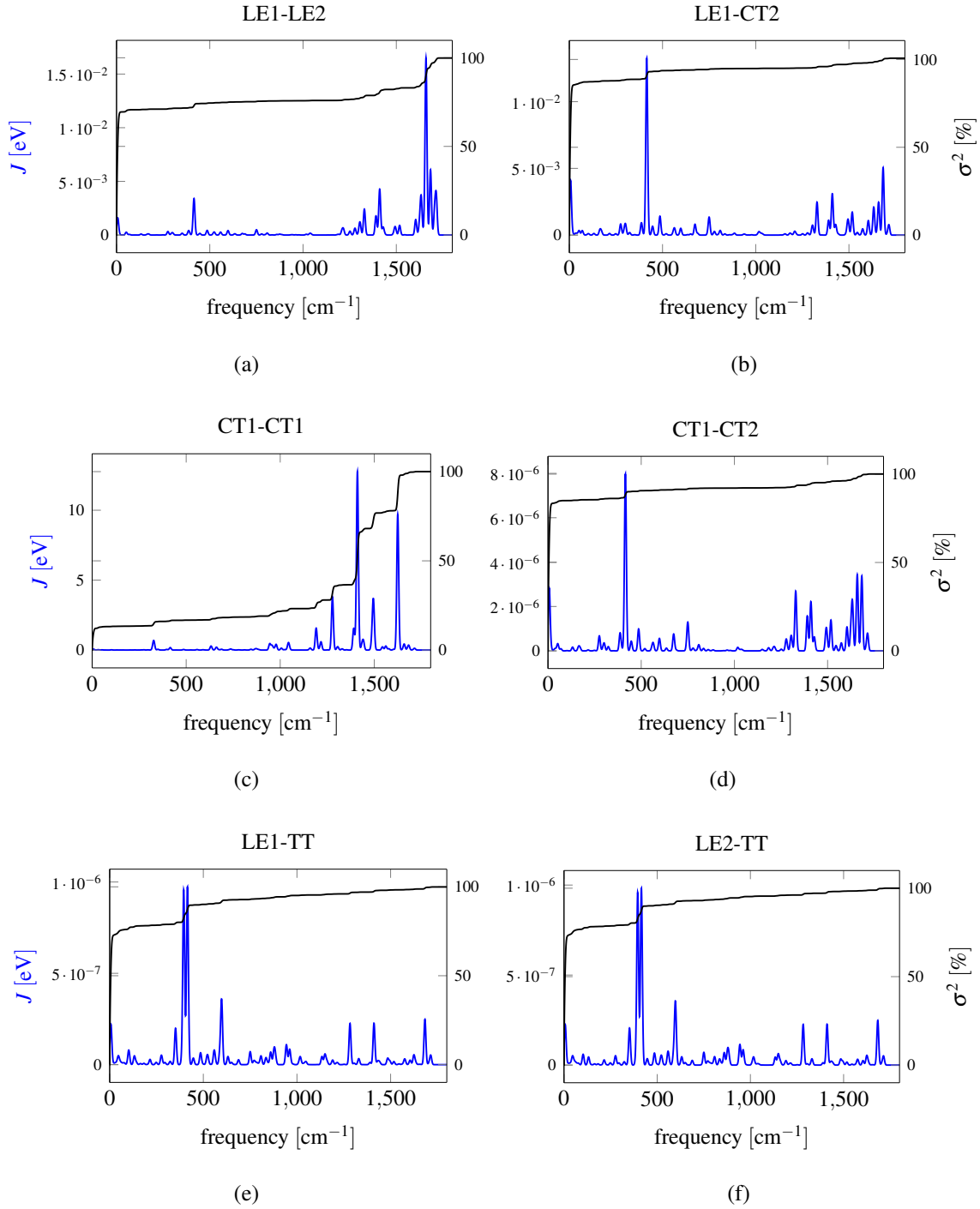


FIG. 8. Spectral density (blue, left axis) and accumulative fluctuations (black, right axis) of selected excitonic Hamiltonian terms at room temperature.

dark initial state almost immediately skyrockets and always satisfies the upper bound. Notice the interesting kink at which the maximum bond dimension drops here for a short time. It is important to mention that only few of the modes actually reached the saturation of the bond dimension limit.

CT energy [eV]	TT population [%]
3.0645	7.72
3.1645	0.43
3.2645	13.8
3.3645	34.78
3.4645	0.04
3.5645	0.02

TABLE II. TT population for different CT energies during the Redfield search.

Typically these are the vibrational modes, whose spectrum decays very slowly, e.g. no. 184 and

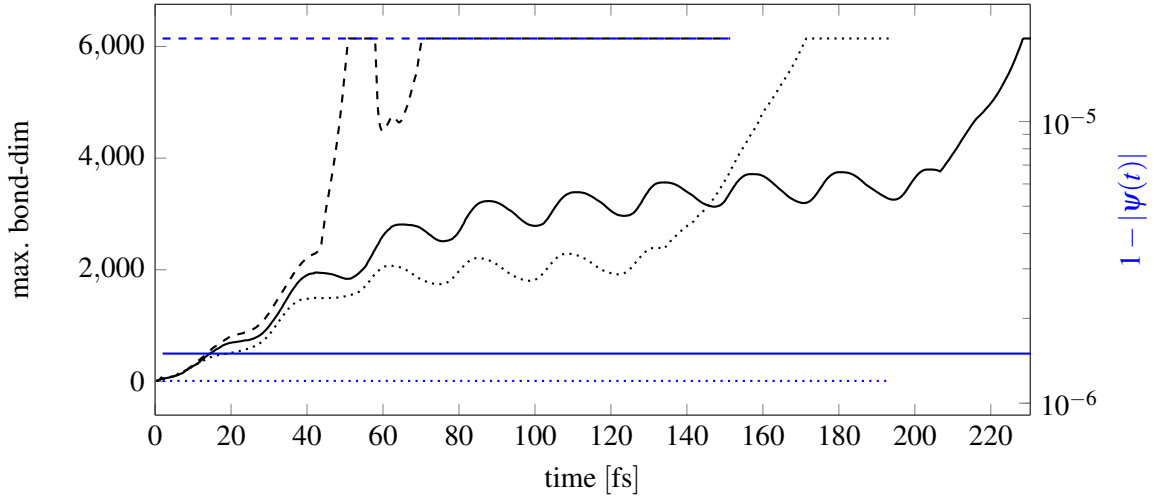


FIG. 9. Numerical control parameters plotted against time. The maximum bond dimension (black) is plotted for the localised (dotted), bright (solid) and dark (dashed) initial state. The breaking of unitarity during the TDVP is observed through the proxy of the initial norm deviation (blue). All of these curves were obtained with $E_{TT} = 2.9493$ eV.

185. Even though the memory requirement depends on the exact model parameters, for those presented in Table I the final wave function (living in a formally $\sim 10^{137}$ dimensional Hilbert space) used only 1.3 GB on the disk. This is to be compared to 32 where the central tensor had a requirement of 57 TB.

TDVP is an inherently local method which is only exact for nearest-neighbour Hamiltonians or infinite bond dimension⁴⁸. Otherwise a so called projection error is introduced, which causes the time evolution to be non-unitary. In order to estimate this error one can look at the deviance from

the initial norm as in Figure 9. As we can recognise the total norm difference is constant throughout the simulation. Furthermore it is in accordance with the truncation error. However it is indeed initial state dependent, i.e. the bright exciton initial state has twice the norm error of the localised one while the dark initial state actually lies one order of magnitude higher. This is explained with regard to the bond dimension, i.e. the phononic modes needing high bond dimensions. Since the TDVP projector is exact for an infinite bond dimension, i.e. for an exact state⁴⁸, the stronger the truncation of the state, the stronger the breaking of unitarity.

Appendix F: Initial state dependence

We investigate the dependency of the excitonic population dynamics on the initial state. To do so we do the time evolution with the excitation localised in one of the chromophores and with an anti-symmetric excitation of both chromophones, as can be seen in Figure 10. It is to mention that the anti-symmetric initial state is dark, i.e. it is not realisable in experiment from the ground state, due to transition rules. We see that for LE initial state $|\psi\rangle(0) = |\text{LE}_1\rangle$ the dynamics is similar to the bright initial state in the main text, i.e. there is also a delay from the CT. However the SF yield is around half of the bright initial state.

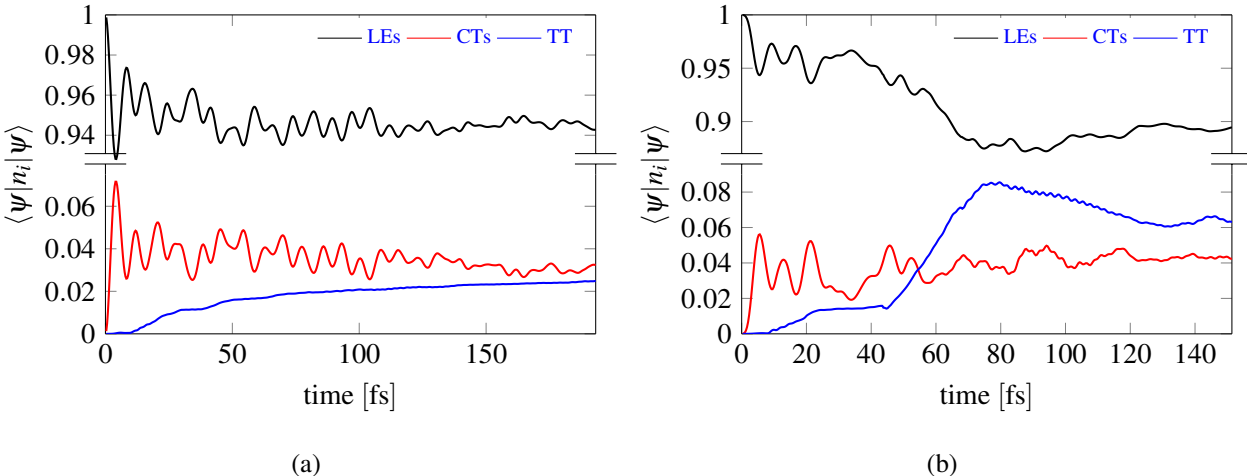


FIG. 10. Electronic population dynamics for different initial states. Figure 10a corresponds to the localized initial state while Figure 10b is the dark one. Both were carried out with $E_{\text{TT}} = 2.9493 \text{ eV}$.

As it was argued before, the mechanism behind the coherent SF is the superposition of the LE and TT state^{64,65}. This is the reason for the small yield of the localized state. It is remarkable to notice that a delocalisation over two chromophores gives a factor of two in the TT yield. This

points into the direction of previous investigations⁹ emphasising the importance of spatial delocalisation. Using the dark initial state we see that a much higher yield than for the system in the main text is reached. After a plateau like region the value approaches $\sim 10\%$. However there is a maximum after which the population begins to decay back mostly into the **LE** states.

Appendix G: Excitonic RDM analysis

In the main text we already discussed the appearance of two different scales characterizing the time evolution of the **TT** occupancy. In order to analyse the origin of these time scales we studied the **RDM** of the excitonic system. In general, the time evolution of the excitonic density operator $\hat{\rho}_{\text{ex}}$ after tracing out the vibrational degrees of freedom can be expanded in its eigenbasis

$$\hat{\rho}_{\text{ex}}(t) = \sum_{i,j \in \mathcal{S}} \langle i | \hat{\rho}_{\text{ex}}(t) | j \rangle | i \rangle \langle j | = \sum_n \lambda_n(t) | \lambda_n(t) \rangle \langle \lambda_n(t) | . \quad (\text{G1})$$

Here, we explicitly exhibited the time-dependence of the eigensystem and defined

$\mathcal{S} = \{\text{TT}, \text{CT}_2, \text{CT}_1, \text{LE}_2, \text{LE}_1\}$. In Figure 11 we show the absolute value of the decomposition

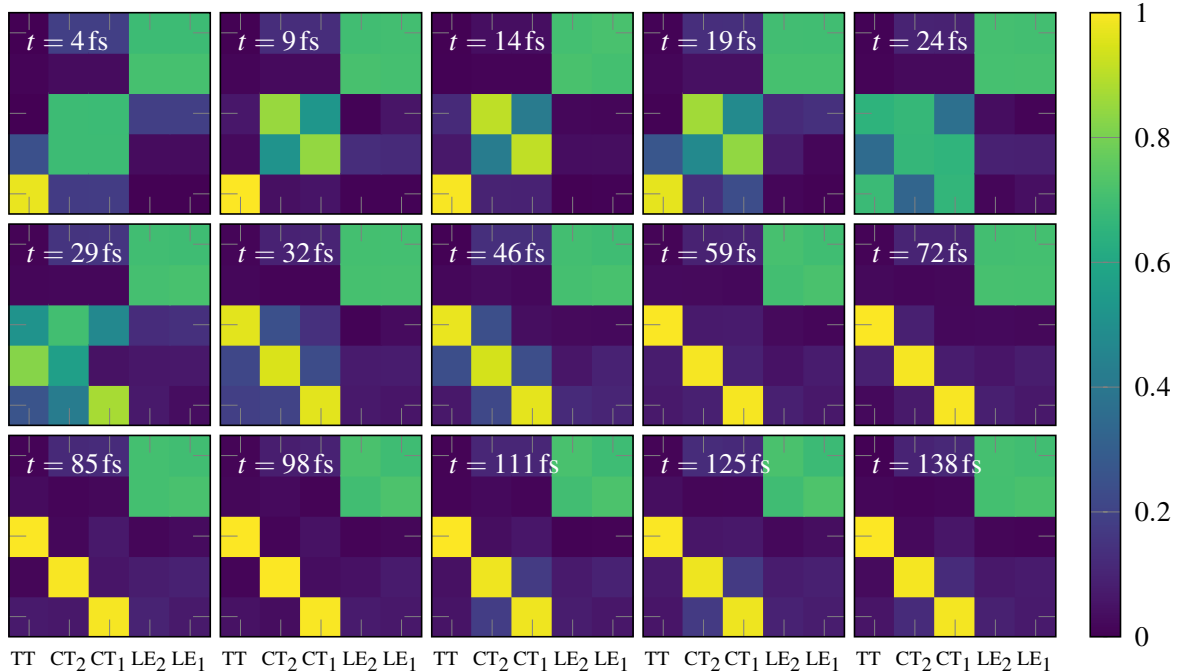


FIG. 11. Time-evolution of the eigenvectors $|\langle \lambda | i \rangle|$ of the electronic **RDM**. $|\lambda\rangle$ enumerates the **RDM** eigenvalues while $|i\rangle \in \{|\text{TT}\rangle, |\text{CT}_2\rangle, |\text{CT}_1\rangle, |\text{LE}_2\rangle, |\text{LE}_1\rangle\}$. Note that the eigenvalues are sorted by magnitude. We count them from top (largest) to bottom (smallest).

of the eigenstates w.r.t. to the excitonic states $|\langle \lambda | i \rangle|$ at different stages during the time evolution. We can clearly identify the timescale $t_0 \approx 30$ fs. At times $t < t_0$ the different eigenvalues of $\hat{\rho}_{\text{ex}}$ are mainly coherent superpositions of the excitonic states. The situation changes significantly at times $t > t_0$. Here, the decomposition of the eigenstates separates into a block-diagonal form. A mixing of excitonic states between the **LE**, **CT** and **TT** subsystems is then only subleading at the order of $\sim 10^{-1}$. Ignoring the weak electronic coherences at $t > t_0$ this implies a decomposition

$$\hat{\rho}_{\text{ex}}(t > t_0) \approx \hat{\rho}_{\text{LE}}(t) \oplus \hat{\rho}_{\text{CT}}(t) \oplus \hat{\rho}_{\text{TT}}(t) = \exp(-(\hat{H}_{\text{LE}}(t) \oplus \hat{H}_{\text{CT}}(t) \oplus \hat{H}_{\text{TT}}(t))t) / Z(t). \quad (\text{G2})$$

In the last equation we introduced effective Hamiltonians governing the time evolution in the different excitonic subsystems:

$$\begin{aligned} \hat{H}_{\text{LE}}(t) = & - \sum_{i,j=1,2} \langle \text{LE}_i | \lambda_4(t) \rangle \log \lambda_4(t) \langle \lambda_4(t) | \text{LE}_j \rangle | \text{LE}_j \rangle \langle \text{LE}_i | \\ & + \langle \text{LE}_i | \lambda_5(t) \rangle \log \lambda_5(t) \langle \lambda_5(t) | \text{LE}_j \rangle | \text{LE}_j \rangle \langle \text{LE}_i | \end{aligned} \quad (\text{G3})$$

$$\hat{H}_{\text{CT}}(t) = -(|\text{CT}_1\rangle \log \lambda_1(t) \langle \text{CT}_1| + |\text{CT}_2\rangle \log \lambda_2(t) \langle \text{CT}_2|) \quad (\text{G4})$$

$$\hat{H}_{\text{TT}}(t) = -|\text{TT}\rangle \log \lambda_3(t) \langle \text{TT}| \quad (\text{G5})$$

Note that due to the normalization of ρ_{ex} we have $\sum_n \lambda_n = 1$. In this decomposition of the excitonic density operator (at times $t > t_0$), the time evolution of the **CTs** and **TT** states is described by the dynamics of a purely mixed state without quantum mechanical coherences. Furthermore, the dynamics of the **LEs** w.r.t. the remaining excitonic states is of the same type and coherent dynamics only happens within the **LEs**. In order to investigate the origin the found electronic coherence time t_0 we rewrite equation Equation (1) by means of a generalised Lang-Firsov-transformation⁶⁶. For that purpose we define a transformation

$$\hat{U} = e^{-\hat{S}}, \quad \hat{S} = \sum_{ij,I} \lambda_{ij,I} \hat{c}_i^\dagger \hat{c}_j \left(\hat{b}_I^\dagger - \hat{b}_I \right), \quad (\text{G6})$$

where $\lambda_{ij,I}$ are real coefficients. These coefficients are now determined such that the exciton phonon couplings are canceled in the transformed Hamiltonian $e^{\hat{S}} \hat{H} e^{-\hat{S}}$. Expansion of the last expression yields:

$$e^{\hat{S}} \hat{H} e^{-\hat{S}} = \hat{H} + [\hat{S}, \hat{H}] + \frac{1}{2} [\hat{S}, [\hat{S}, \hat{H}]] + \dots \quad (\text{G7})$$

After some algebra the commutator evaluates to

$$\begin{aligned}
[\hat{S}, \hat{H}] &= \sum_{ij,I} \hat{c}_i^\dagger \hat{c}_j (A_{ij,I} - A_{ji,I}) (\hat{b}_I^\dagger - \hat{b}_I) - \sum_{ij,I} \lambda_{ij,I} \omega_I \hat{c}_i^\dagger \hat{c}_j (\hat{b}_I^\dagger + \hat{b}_I) \\
&\quad + \sum_{ij,IJ} \hat{c}_i^\dagger \hat{c}_j (B_{ij,IJ} - B_{ji,IJ}) (\hat{b}_I^\dagger + \hat{b}_I) (\hat{b}_J^\dagger - \hat{b}_J) - 2 \sum_{ijkl} \Omega_{ijkl} \hat{c}_i^\dagger \hat{c}_j \hat{c}_k^\dagger \hat{c}_l, \quad (\text{G8})
\end{aligned}$$

where we defined $\lambda_{ij,I} = \frac{g_{ij,I}}{\omega_I}$ that generates the desired cancellation of the exciton-phonon interaction term as well as

$$A_{ij,I} = \frac{1}{\omega_I} \sum_k g_{ik,I} V_{kj}, \quad B_{ij,IJ} = \frac{1}{\omega_I} \sum_k g_{ik,I} g_{kj,J} \quad \text{and} \quad \Omega_{ijkl} = \sum_I \frac{g_{ij,I} g_{kl,I}}{\omega_I}. \quad (\text{G9})$$

Furthermore $A_{ij,I}$ and $B_{ij,IJ}$ are symmetric matrices in the excitonic indices i and j . Thus the commutator of the generator with the Hamiltonian becomes

$$[\hat{S}, \hat{H}] = - \sum_{ij,I} g_{ij,I} \hat{c}_i^\dagger \hat{c}_j (\hat{b}_I^\dagger + \hat{b}_I) - 2 \sum_{ijkl} \Omega_{ijkl} \hat{c}_i^\dagger \hat{c}_j \hat{c}_k^\dagger \hat{c}_l. \quad (\text{G10})$$

In the following, higher order commutators including the quartic excitonic coupling term are neglected since Ω_{ijkl} is subleading. We thus obtain

$$e^{\hat{S}} \hat{H} e^{-\hat{S}} \approx \sum_{ij} V_{ij} \hat{c}_i^\dagger \hat{c}_j + \sum_I \omega_I \hat{b}_I^\dagger \hat{b}_I - 2 \sum_{ijkl} \Omega_{ijkl} \hat{c}_i^\dagger \hat{c}_j \hat{c}_k^\dagger \hat{c}_l. \quad (\text{G11})$$

Transforming back into the exciton-phonon basis we arrive at

$$\hat{H} \approx \sum_{ij} V_{ij} e^{-\hat{S}} \hat{c}_i^\dagger \hat{c}_j e^{\hat{S}} + \sum_I \omega_I e^{-\hat{S}} \hat{b}_I^\dagger \hat{b}_I e^{\hat{S}} - 2 \sum_{ijkl} \Omega_{ijkl} e^{-\hat{S}} \hat{c}_i^\dagger \hat{c}_j \hat{c}_k^\dagger \hat{c}_l e^{\hat{S}}. \quad (\text{G12})$$

Now we focus on the renormalisation of the exciton coupling matrix elements V_{ij} . For that purpose we write the exponential in the eigenbasis of the excitonic part of the generator coefficients $\lambda_{ij,I} = \frac{g_{ij,I}}{\omega_I}$:

$$\exp \left(\sum_I \hat{c}^\dagger \Lambda_I \hat{c} (\hat{b}_I^\dagger - \hat{b}_I) \right) = \exp \left(\sum_I \hat{\mathbf{f}}_I^\dagger D_I \hat{\mathbf{f}}_I (\hat{b}_I^\dagger - \hat{b}_I) \right). \quad (\text{G13})$$

In the last line we defined $\hat{\mathbf{c}}^\dagger = (\hat{c}_{\text{LE}1}^\dagger, \hat{c}_{\text{LE}2}^\dagger, \dots)$, $D_I = R_I \Lambda_I R_I^\dagger$ with orthogonal matrices R_I and rotated excitonic operators $\hat{\mathbf{f}}_I^\dagger = \hat{\mathbf{c}}^\dagger R_I^\dagger$. Reinserting this expansion into the excitonic coupling term of Equation (G12) yields

$$V_{ij} e^{-\hat{S}} \hat{c}_i^\dagger \hat{c}_j e^{\hat{S}} = \exp \left(- \sum_I \hat{\mathbf{f}}_I^\dagger D_I \hat{\mathbf{f}}_I (\hat{b}_I^\dagger - \hat{b}_I) \right) V_{ij} \hat{c}_i^\dagger \hat{c}_j \exp \left(\sum_I \hat{\mathbf{f}}_I^\dagger D_I \hat{\mathbf{f}}_I (\hat{b}_I^\dagger - \hat{b}_I) \right) \quad (\text{G14})$$

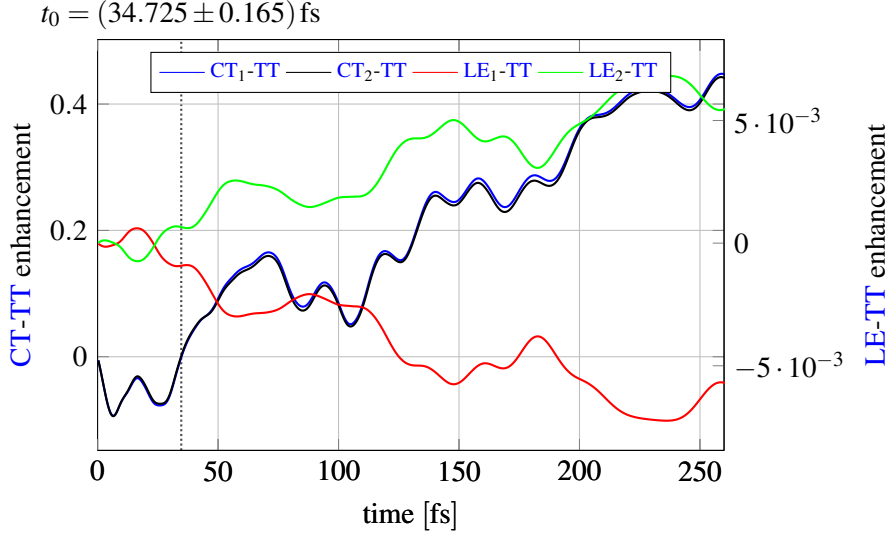


FIG. 12. Summed up transformation matrix elements corresponding to transitions into the **TT** state. The sign change indicates a transition from enhanced to suppressed hoppings.

For each exciton-phonon coupling matrix Λ_I we computed the eigenvalues which we found to be strictly positive. Additionally, each element of $\hat{\mathbf{f}}_I^\dagger \hat{\mathbf{f}}_I$ is between zero and one. As a consequence, an enhancement (positive overall exponent) or suppression (negative overall exponent) of the hoppings can be identified by evaluating the momentum expectation values $\propto i(\hat{b}_I^\dagger - \hat{b}_I)$. In Figure 12 we show the expectation value of the hopping matrix renormalisation corresponding to transitions into the **TT** state

$$\langle \psi(t) | \sum_I \lambda_{\mathbf{TT}j,i} i(\hat{b}_I^\dagger - \hat{b}_I) | \psi(t) \rangle \quad \text{with } j = \mathbf{LE}_1, \mathbf{LE}_2, \mathbf{CT}_1, \mathbf{CT}_2 \quad (\text{G15})$$

We find a change of sign at a simulation time $t_0 = 34.725$ fs. Note that for $t < t_0$ we observe a negative sign in the dominating matrix elements corresponding to hopping from the **CT** into the **TT** state indicating an enhancement of the transition amplitude. For $t > t_0$ the situation changes into the opposite and hoppings into the **TT** state are suppressed. Importantly, we also find a nearly vanishing renormalization for the direct path **LE** \rightarrow **TT**. This emphasises the significant role played by the super exchange path in the **TT** production during the coherent dynamics.

REFERENCES

- ¹A. F. Morrison and J. M. Herbert, *J. Phys. Chem. Lett* **8**, 1442 (2017), pMID: 28277682, <https://doi.org/10.1021/acs.jpcclett.7b00230>.

- ²M. B. Smith and J. Michl, *Chem. Rev.* **110**, 6891 (2010), pMID: 21053979, <https://doi.org/10.1021/cr1002613>.
- ³D. Casanova, *Chem. Rev.* **118**, 7164 (2018), pMID: 29648797, <https://doi.org/10.1021/acs.chemrev.7b00601>.
- ⁴P. M. Zimmerman, Z. Zhang, and C. B. Musgrave, *Nat. Chem.* **2**, 648 (2010).
- ⁵H. Najafov, B. Lee, Q. Zhou, L. C. Feldman, and V. Podzorov, *Nat. Mater.* **9**, 938 (2010).
- ⁶P. Irkhin and I. Biaggio, *Phys. Rev. Lett.* **107**, 017402 (2011).
- ⁷D. N. Congreve, J. Lee, N. J. Thompson, E. Hontz, S. R. Yost, P. D. Reusswig, M. E. Bahlke, S. Reineke, T. Van Voorhis, and M. A. Baldo, *Science* **340**, 334 (2013), <https://science.sciencemag.org/content/340/6130/334.full.pdf>.
- ⁸M. C. Hanna and A. J. Nozik, *J. Appl. Phys.* **100**, 074510 (2006), <https://doi.org/10.1063/1.2356795>.
- ⁹Z. Wang, H. Liu, X. Xie, C. Zhang, R. Wang, L. Chen, Y. Xu, H. Ma, W. Fang, Y. Yao, H. Sang, X. Wang, X. Li, and M. Xiao, *Nat. Chem.* **13**, 559 (2021).
- ¹⁰H. Tamura, M. Huix-Rotllant, I. Burghardt, Y. Olivier, and D. Beljonne, *Phys. Rev. Lett.* **115**, 107401 (2015).
- ¹¹J. Zheng, Y. Xie, S. Jiang, and Z. Lan, *J. Phys. Chem. C* **120**, 1375 (2016), <https://doi.org/10.1021/acs.jpcc.5b09921>.
- ¹²S. R. Reddy, P. B. Coto, and M. Thoss, *J. Phys. Chem. Lett.* **9**, 5979 (2018), <https://doi.org/10.1021/acs.jpcllett.8b02674>.
- ¹³W.-L. Chan, T. C. Berkelbach, M. R. Provorse, N. R. Monahan, J. R. Tritsch, M. S. Hybertsen, D. R. Reichman, J. Gao, and X.-Y. Zhu, *Acc. Chem. Res.* **46**, 1321 (2013), pMID: 23581494, <https://doi.org/10.1021/ar300286s>.
- ¹⁴G. Tao, *J. Chem. Phys.* **151**, 054308 (2019), <https://doi.org/10.1063/1.5100196>.
- ¹⁵H. Zang, Y. Zhao, and W. Liang, *J. Phys. Chem. Lett.* **8**, 5105 (2017), pMID: 28960999, <https://doi.org/10.1021/acs.jpcllett.7b01996>.
- ¹⁶X. Xie, A. Santana-Bonilla, W. Fang, C. Liu, A. Troisi, and H. Ma, *J. Chem. Theory Comput.* **15**, 3721 (2019), pMID: 30970207, <https://doi.org/10.1021/acs.jctc.9b00122>.
- ¹⁷H. Tamura, M. Huix-Rotllant, I. Burghardt, Y. Olivier, and D. Beljonne, *Phys. Rev. Lett.* **115**, 107401 (2015).
- ¹⁸N. R. Monahan, D. Sun, H. Tamura, K. W. Williams, B. Xu, Y. Zhong, B. Kumar, C. Nuckolls, A. R. Harutyunyan, G. Chen, H.-L. Dai, D. Beljonne, Y. Rao, and X. Y. Zhu, *Nat. Chem.* **9**, 341

- (2017).
- ¹⁹E. Busby, J. Xia, Q. Wu, J. Z. Low, R. Song, J. R. Miller, X. Y. Zhu, L. M. Campos, and M. Y. Sfeir, *Nat. Mater.* **14**, 426 (2015).
- ²⁰K. Miyata, Y. Kurashige, K. Watanabe, T. Sugimoto, S. Takahashi, S. Tanaka, J. Takeya, T. Yanai, and Y. Matsumoto, *Nat. Chem.* **9**, 983 (2017).
- ²¹A. A. Bakulin, S. E. Morgan, T. B. Kehoe, M. W. B. Wilson, A. W. Chin, D. Zigmantas, D. Egorova, and A. Rao, *Nat. Chem.* **8**, 16 (2016).
- ²²R. Tempelaar and D. R. Reichman, *J. Chem. Phys.* **146**, 174703 (2017), <https://doi.org/10.1063/1.4982362>.
- ²³U. Manthe, H. Meyer, and L. S. Cederbaum, *J. Chem. Phys.* **97**, 3199 (1992), <https://doi.org/10.1063/1.463007>.
- ²⁴H.-D. Meyer, U. Manthe, and L. Cederbaum, *Chem. Phys. Lett.* **165**, 73 (1990).
- ²⁵M. Beck, A. Jäckle, G. Worth, and H.-D. Meyer, *Phys. Rep.* **324**, 1 (2000).
- ²⁶A. REDFIELD, in *Adv. Magn. Reson.*, Advances in Magnetic and Optical Resonance, Vol. 1, edited by J. S. Waugh (Academic Press, 1965) pp. 1–32.
- ²⁷D. Egorova, M. Thoss, W. Domcke, and H. Wang, *J. Chem. Phys.* **119**, 2761 (2003), <https://doi.org/10.1063/1.1587121>.
- ²⁸L. Han, Y. Ke, X. Zhong, and Y. Zhao, *Int. J. Quantum Chem.* **115**, 578 (2015), <https://onlinelibrary.wiley.com/doi/pdf/10.1002/qua.24833>.
- ²⁹S. R. Reddy, P. B. Coto, and M. Thoss, *The Journal of Chemical Physics* **151**, 044307 (2019), <https://doi.org/10.1063/1.5109897>.
- ³⁰U. Manthe, *J. Chem. Phys.* **128**, 164116 (2008), <https://doi.org/10.1063/1.2902982>.
- ³¹U. Manthe, *J. Chem. Phys.* **130**, 054109 (2009), <https://doi.org/10.1063/1.3069655>.
- ³²F. A. Y. N. Schröder, D. H. P. Turban, A. J. Musser, N. D. M. Hine, and A. W. Chin, *Nature Communications* **10**, 1062 (2019).
- ³³T. Köhler, J. Stolpp, and S. Paeckel, *SciPost Phys.* **10**, 58 (2021).
- ³⁴J. Frenkel, *Phys. Rev.* **37**, 17 (1931).
- ³⁵J. Frenkel, *Phys. Rev.* **37**, 1276 (1931).
- ³⁶K. Miyata, F. S. Conrad-Burton, F. L. Geyer, and X.-Y. Zhu, *Chem. Rev.* **119**, 4261 (2019), <https://doi.org/10.1021/acs.chemrev.8b00572>.
- ³⁷R. C. Johnson and R. E. Merrifield, *Phys. Rev. B* **1**, 896 (1970).

- ³⁸N. J. Mayhall, *J. Chem. Theory Comput.* **12**, 4263 (2016), pMID: 27472260, <https://doi.org/10.1021/acs.jctc.6b00545>.
- ³⁹A. Shabaev, A. L. Efros, and A. J. Nozik, *Nano Lett.* **6**, 2856 (2006), pMID: 17163719, <https://doi.org/10.1021/nl062059v>.
- ⁴⁰E. A. Buchanan and J. Michl, *J. Am. Chem. Soc.* **139**, 15572 (2017), pMID: 29039927, <https://doi.org/10.1021/jacs.7b07963>.
- ⁴¹T. C. Berkelbach, M. S. Hybertsen, and D. R. Reichman, *J. Chem. Phys.* **138**, 114102 (2013), <https://doi.org/10.1063/1.4794425>.
- ⁴²T. C. Berkelbach, M. S. Hybertsen, and D. R. Reichman, *J. Chem. Phys.* **138**, 114103 (2013), <https://doi.org/10.1063/1.4794427>.
- ⁴³S. Lukman, K. Chen, J. M. Hodgkiss, D. H. P. Turban, N. D. M. Hine, S. Dong, J. Wu, N. C. Greenham, and A. J. Musser, *Nat. Commun.* **7**, 13622 (2016).
- ⁴⁴E. A. Margulies, C. E. Miller, Y. Wu, L. Ma, G. C. Schatz, R. M. Young, and M. R. Wasielewski, *Nat. Chem.* **8**, 1120 (2016).
- ⁴⁵J. C. Johnson, A. J. Nozik, and J. Michl, *Acc. Chem. Res.* **46**, 1290 (2013).
- ⁴⁶U. Schollwöck, *Rev. Mod. Phys.* **77**, 259 (2005).
- ⁴⁷U. Schollwöck, *Ann. Phys.* **326**, 96 (2011).
- ⁴⁸S. Paeckel, T. Köhler, A. Swoboda, S. R. Manmana, U. Schollwöck, and C. Hubig, *Ann. Phys.* **411**, 167998 (2019).
- ⁴⁹J. Haegeman, J. I. Cirac, T. J. Osborne, I. Pižorn, H. Verschelde, and F. Verstraete, *Phys. Rev. Lett.* **107**, 070601 (2011).
- ⁵⁰J. Haegeman, C. Lubich, I. Oseledets, B. Vandereycken, and F. Verstraete, *Physical Review B* **94**, 165116 (2016).
- ⁵¹C. Hubig, F. Lachenmaier, N.-O. Linden, T. Reinhard, L. Stenzel, A. Swoboda, M. Grundner, and S. Mardazad, “The SYTEN toolkit,” .
- ⁵²J. Stolpp, T. Koehler, S. R. Manmana, E. Jeckelmann, F. Heidrich-Meisner, and S. Paeckel, *Computer Physics Communications* , 108106 (2021).
- ⁵³S. Singh, R. N. C. Pfeifer, and G. Vidal, *Phys. Rev. B* **83** (2011), 10.1103/physrevb.83.115125.
- ⁵⁴P. Secular, N. Gourianov, M. Lubasch, S. Dolgov, S. R. Clark, and D. Jaksch, *Phys. Rev. B* **101**, 235123 (2020).
- ⁵⁵E. Jeckelmann and S. R. White, *Phys. Rev. B* **57**, 6376 (1998).
- ⁵⁶C. Zhang, E. Jeckelmann, and S. R. White, *Phys. Rev. B* **60**, 14092 (1999).

- ⁵⁷C. Zhang, E. Jeckelmann, and S. R. White, *Phys. Rev. Lett.* **80**, 2661 (1998).
- ⁵⁸C. Brockett, F. Dorfner, L. Vidmar, F. Heidrich-Meisner, and E. Jeckelmann, *Phys. Rev. B* **92**, 241106 (2015).
- ⁵⁹F. Dorfner, L. Vidmar, C. Brockett, E. Jeckelmann, and F. Heidrich-Meisner, *Phys. Rev. B* **91**, 104302 (2015).
- ⁶⁰J. Stolpp, J. Herbrych, F. Dorfner, E. Dagotto, and F. Heidrich-Meisner, *Phys. Rev. B* **101**, 035134 (2020).
- ⁶¹C. Hubig, I. P. McCulloch, and U. Schollwöck, *Physical Review B* **95** (2017), 10.1103/physrevb.95.035129.
- ⁶²S. Mukamel, *Principles of Nonlinear Optical Spectroscopy* (Oxford University Press, New York, 1995).
- ⁶³L. Xue, X. Song, Y. Feng, S. Cheng, G. Lu, and Y. Bu, *J. Am. Chem. Soc.* **142**, 17469 (2020), pMID: 32927954, <https://doi.org/10.1021/jacs.0c06919>.
- ⁶⁴W.-L. Chan, M. Ligges, A. Jailaubekov, L. Kaake, L. Miaja-Avila, and X.-Y. Zhu, *Science* **334**, 1541 (2011), <https://science.sciencemag.org/content/334/6062/1541.full.pdf>.
- ⁶⁵N. Monahan and X.-Y. Zhu, *Ann. Rev. Phys. Chem.* **66**, 601 (2015), pMID: 25648486, <https://doi.org/10.1146/annurev-physchem-040214-121235>.
- ⁶⁶I. Lang and Y. A. Firsov, *Sov. Phys. JETP* **16**, 1301 (1963).
- ⁶⁷S. Paeckel and T. Köhler, “Symmps,” <https://www.symmps.eu>, accessed: 2019-12-29.
- ⁶⁸J. Pipek and P. G. Mezey, *J. Chem. Phys.* **90**, 4916 (1989), <https://doi.org/10.1063/1.456588>.
- ⁶⁹I. Fdez. Galvan, M. Vacher, A. Alavi, C. Angeli, F. Aquilante, J. Autschbach, J. J. Bao, S. I. Bokarev, N. A. Bogdanov, R. K. Carlson, L. F. Chibotaru, J. Creutzberg, N. Dattani, M. G. Delcey, S. S. Dong, A. Dreuw, L. Freitag, L. M. Frutos, L. Gagliardi, F. Gendron, A. Giussani, L. Gonzalez, G. Grell, M. Guo, C. E. Hoyer, M. Johansson, S. Keller, S. Knecht, G. Kovacevic, E. Kaellman, G. Li Manni, M. Lundberg, Y. Ma, S. Mai, J. P. Malhado, P. A. Malmqvist, P. Marquetand, S. A. Mewes, J. Norell, M. Olivucci, M. Oppel, Q. M. Phung, K. Pierloot, F. Plasser, M. Reiher, A. M. Sand, I. Schapiro, P. Sharma, C. J. Stein, L. K. Sorensen, D. G. Truhlar, M. Ugandi, L. Ungur, A. Valentini, S. Vancoillie, V. Veryazov, O. Weser, T. A. Wesolowski, P.-O. Widmark, S. Wouters, A. Zech, J. P. Zobel, and R. Lindh, *J. Chem. Theory Comput.* **15**, 5925 (2019), pMID: 31509407, <https://doi.org/10.1021/acs.jctc.9b00532>.